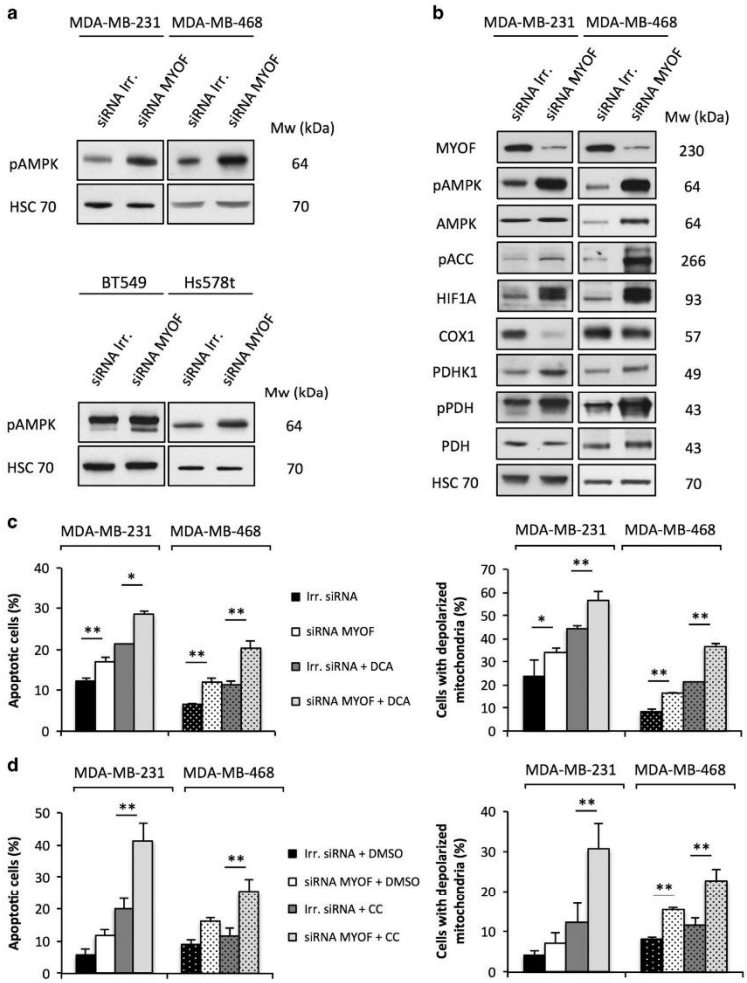

Figure 5. Myoferlin silencing activates AMPK and sensitizes cells to drugs targeting metabolism. (**a**) Western blot analysis of different TNBC cell lines showed that AMPK activation is a consistent feature of myoferlin depletion. (**b**) Western blot analysis of different metabolic proteins in MDA-MB231 and MDA-MB-468 cells. (**a** and **b**) Representative images of three independent experiments; HSC70 was used as a loading control. (**c**, **d**) Apoptosis induction (left panel) and TMRE accumulation (right panel) following myoferlin silencing in MDA-MB-231 and MDA-MB-468. DCA and compound C treatments both enhanced cell death upon myoferlin silencing. Error bars indicate s.d. of means from minimum three independent biological replicates. Statistical significance (*P*) was evaluated using an unpaired Student *t*-test (**P*-value $\leqslant$ 0.05; ***P*-value $\leqslant$ 0.01).

Myoferlin suppression lowers metastatic propensity of TNBC cells *in vivo* and low myoferlin expression correlates with better clinical outcome

For the purpose of assessing tumoral progression *in vivo*, mice xenografted with MDA-MB-231 were first operated to remove primary tumors, and then assessed for metastasis formation. Magnetic resonance imaging of the mice 2 weeks after surgery showed that majority of control mice developed lymph node infiltrates and overt lung metastasis (Figure 7a). In contrast to this, mice operated from myoferlin-silenced tumors demonstrated lower lymph node infiltration and no sign of evident lung metastasis (Figure 7a). Four weeks post tumor resection, the mice were sacrificed and the lungs were subjected to histological evaluation. We evaluated serial sections of the entire lungs for

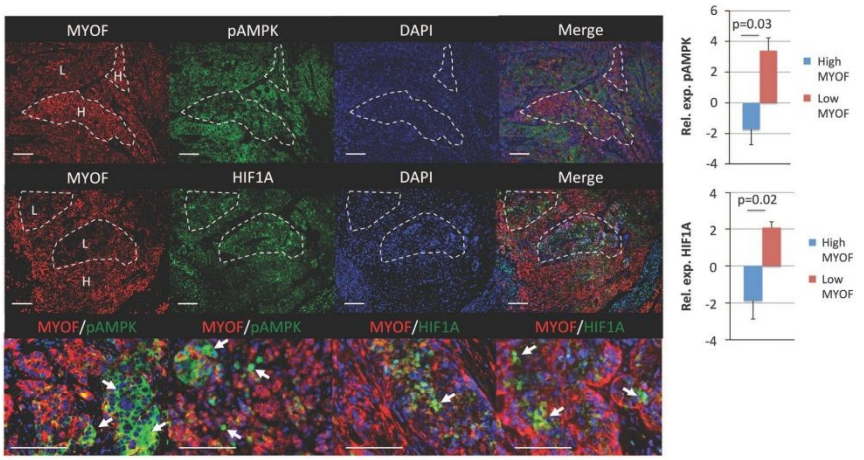

Figure 6. AMPK activation and HIF1A stabilization negatively correlate with myoferlin expression in breast cancer tissues. Immunofluorescence analysis of AMPK phosphorylation/activation and HIF1 stabilization in TNBC patients ($N = 10$). Quantification of pAMPK and HIF1A intensity in regions with low and high MYOF confirmed a significant inverse relationship between MYOF and pAMPK/HIF1A. High-power view: groups of cells that expressed high MYOF but low pAMPK/HIF1A levels and vice versa. Error bars indicate s.d. Statistical significance (P) was evaluated using an unpaired Student t-test.

tumoral foci using human vimentin staining. The results showed that control mice bearing wild-type tumors had indeed developed more frequent and larger metastatic foci than the mice with myoferlin-depleted tumors (Figure 7b). Encouraged by these findings in animal model we next sought to examine the situation in humans (Figures 7c and d). For this purpose we have used two independent patient cohorts; a smaller one (Figure 7c, $N = 39$) where myoferlin expression was assessed at protein level and a larger one (Figure 7d, $N = 219$) where gene expression data were available. The assessment of the clinical outcome in the first cohort revealed that TNBC patients with myoferlin overexpressing tumors had significantly poorer 10-year outcome (overall survival) (Figure 7c). The analysis of the second patient cohort reinforced these findings (Figure 7d). The high expression of myoferlin mRNA in basal-like tumors correlated with worst distant metastasis-free and overall survival (hazard ratio = 2.26, $P = 0.0098$ and hazard ratio = 2.63, $P = 0.0025$).

DISCUSSION

TNBC remains the subtype of breast cancer with the worst clinical outcome. Identification and functional characterization of new targets and mechanisms contributing to the progression of TNBC represents, therefore, a major research priority. The present study highlights the predominant expression of myoferlin in TNBC, a novel physiologically important protein turned into oncogene in many human cancers.[19–26] Despite myoferlins' emerging role in tumor biology, we know only very little about the underlying mechanisms. The current study demonstrates for the first time that myoferlin silencing in TNBC reduces tumor growth and metastatic progression by significantly deregulating cellular metabolism. Cellular metabolism is tightly regulated by the intake of nutrients and external signals mediated by growth factors. Vesicle traffic in specific and endosomal system, in general, are keys to both nutrient uptake and internalization of activated growth factor receptors. We have previously shown in breast cancer cells that myoferlin controls the handling of internalized epidermal growth factor receptor.[20] In normal muscle and endothelial cells myoferlin has been shown as relevant for cell–cell fusion and endocytosis.[27,28,33] In the present study, our proteomic analysis of myoferlin-deficient tumors highlighted perturbation of vesicle transport and metabolic proteins, whereas electron microscopy results evidenced vesicle accumulation inside myoferlin-depleted cells. Collectively these data suggested a link between the oncogenic function of myoferlin and cellular metabolism. This was further supported by metabolomic analysis of myoferlin-depleted tumors. The results demonstrated a significant downregulation of several intermediates of the tricarboxylic acid cycle as well as derivatives of essential polyunsaturated fatty acids (for example, linoleic acid and arachidonic acid). *In vitro*, myoferlin depletion in breast cancer cells led to significant intracellular accumulation of lipid-based compounds and abundant fatty acids, shifting the sensitive cellular balance between saturated and unsaturated fats. The observed deregulation of lipid metabolism was likely caused by the stalled vesicle traffic that is known to be the key to lipid trafficking. In the present work we were unable to further clarify how myoferlin caused stalled vesicle traffic, resulting in the evident reduction of the late endosomes. This aspect should, therefore, be elucidated in future studies as it could potentially represent a druggable mechanism. Along these lines, the misbalance of fatty acids could additionally be provoked by the known destabilizing effects myoferlin has upon caveolae.[20,28] The mechanism how myoferlin structurally affects caveolae is also not understood. However, caveolae are frequently referred to as 'fat caves' and are as such important for regulating cholesterol and fatty acid homeostasis in the cell.[34] The mitochondrial function is highly sensitive to modulations in cellular lipids and fatty acids. We have, thus, hypothesized that the observed fatty acid alterations must have an impact on mitochondrial function. Indeed, decreased OXPHOS and ATP levels in TNBC cells were some of the most palpable changes caused by myoferlin suppression. Cancer cells responded to the new situation by reprogramming their metabolism toward glycolysis.[35] A key

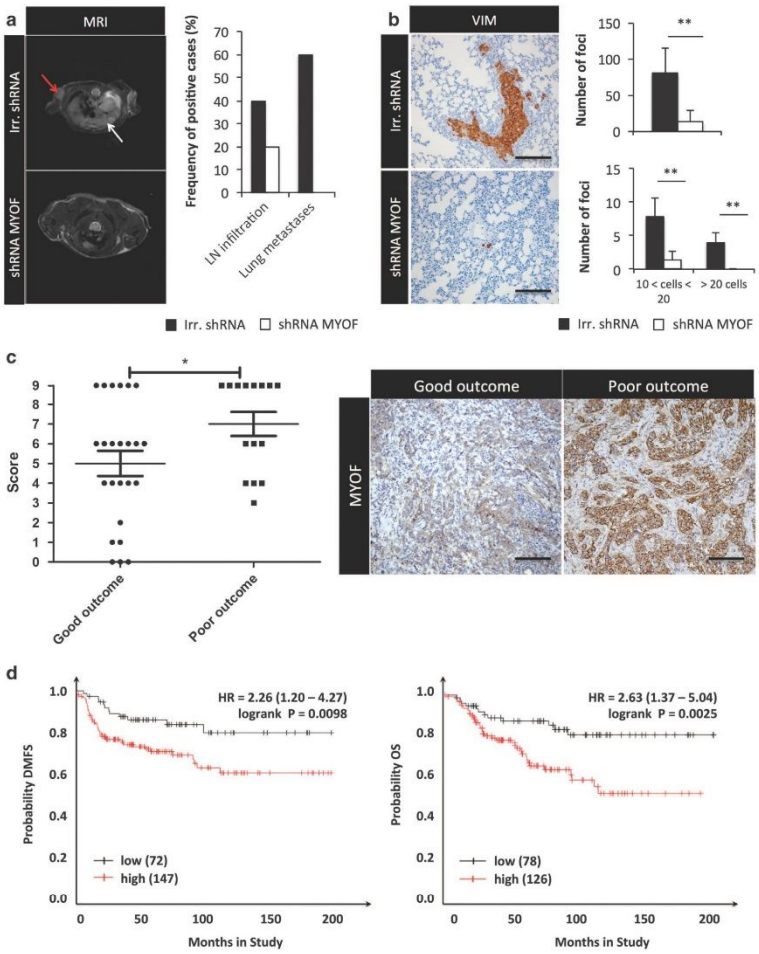

Figure 7. Myoferlin silencing reduces metastasis formation *in vivo*, whereas low myoferlin tumor levels signify better clinical outcome. (**a**) Magnetic resonance imaging (MRI) quantification of lung metastasis formation performed 2 weeks after primary tumor resection. In contrast to control, tumor xenografts lacking myoferlin displayed fewer lymph node infiltration (red arrow) and lung metastases (white arrow). (**b**) Immunohistochemistry (IHC) evaluation of vimentin in lung necropsies and quantification of metastatic deposits (4 weeks). Error bars indicate s.d. of means ($N = 10$ animals). Statistical significance (P) was evaluated using an unpaired Student t-test (**P-value $\leqslant 0.01$). (**c**) IHC analysis of myoferlin expression in a cohort of TNBC patients with different 10-year clinical outcomes (overall survival (OS)) ($N = 39$). Representative IHC pictures of myoferlin-stained tumors from good and bad outcome patients (100-fold magnification). Error bars indicate s.e. of means ($N = 24$ good and $N = 15$ poor outcome). Statistical significance (P) was evaluated using Mann–Whitney U-test (*P-value $\leqslant 0.05$). (**d**) Kaplan–Meier distant metastasis-free (DMFS) and OS curves of patients with basal-like tumors expressing high or low myoferlin mRNA; adapted from KM plotter: http://kmplot.com.

protein enabling this adaptation is AMPK, which is the kinase sensing ATP levels and regulating energy homeostasis. The metabolic reprogramming following myoferlin depletion was further characterized by the inhibition of PDH and stabilization of HIF1A. Therefore it is not far reached to assume that activation of AMPK and increased Warburg effect are initial adaptive measures for cancer cells to escape apoptosis. Blocking this rescue mechanism, by forcing the cells to produce energy through OXPHOS or by inhibiting AMPK phosphorylation, would significantly increase cell death. Indeed, forcing the metabolism

through Krebs cycle or inhibiting AMPK activity both resulted in increased apoptosis and mitochondrial stress (depolarization) in conjunction with myoferlin silencing.

Despite the fact that glycolysis has been long regarded as hallmark of cancer cells and a factor that positively correlates with aggressiveness,[36] the ability of cancer cell to switch to OXPHOS is increasingly seen as a key to tumor progression. For example, recent data by LeBleu *et al.*[37] elegantly show that circulating cancer cells switch their metabolism to OXPHOS and increase mitochondrial biogenesis for augmenting ATP production. Acquisition of a metastatic phenotype has been demonstrated to be dependent on increased mitochondrial metabolism and mediated by higher levels of mitochondrial ROS.[38] Therefore the process of metastasis necessitates metabolic flexibility in cancer cells enabling them to switch from glycolysis to OXPHOS and vice versa.[39,40] Considering the above said, we hypothesized that loss of myoferlin would result in decreased metastases formation. This hypothesis was verified in an *in vivo* model of lung metastases development, demonstrating for the first time that mice bearing myoferlin-depleted tumors develop significantly fewer and smaller lung lesions than the control cohort. Our immunohistochemistry (IHC) analysis on patient specimen confirms the observation made in animal xenograft-based model of metastasis as clinically relevant. Patients with TNBC tumors expressing high levels of myoferlin have significantly shorter 10-year survival than patients with tumors expressing lower myoferlin levels. Independent cohorts confirm this finding also at the mRNA level, underlying the correlation of high myoferlin mRNA levels and poor clinical outcome in basal-like breast tumors.

The current study highlights myoferlin as an understudied oncogene, which now provides an important missing link between the endosomal system and metabolism on one side and tumor progression on the other. Next to addressing the open mechanistic questions, future studies should also aim to identify the peptide domains within myoferlin that are important for its structural and functional role in cancer. This information may offer the possibility to pharmacologically act on myoferlin in order to destabilize the protein in cancer cells.

MATERIALS AND METHODS

Patients

The ethical committee of the University Hospital Liege has approved the use of human material in the current study. All samples were obtained from the institutional biobank of the University Hospital Liege, Belgium, and the study design was based on the retrospective study of the material. According to Belgian law, patients obtained the information that the residual material could be used for research purpose and the consent is presumed as long as the patient does not oppose (opting-out). The initial IHC analysis of myoferlin expression was performed on 30 breast cancer patients of TNBC subtypes. Correlation of myoferlin expression with patient outcome (overall survival) was conducted on a separate series of 39 patients (10-year follow-up). Overall, the TNBC patients involved in the present study had an average age of 65, tumor size of 27 mm (diameter), were of Bloom grade 3, had Ki67 positivity of 47% and frequency of lymph node infiltration of 32%. No power analysis was used to determine the size of the patient cohort. The patients were selected based on material availability and clinical follow-up.

Cell culture, siRNA- and shRNA-mediated knockdown

Breast cancer cell lines (MDA-MB-231 (HTB-26)/ MDA-MB-468 (HTB-132)/ BT-549 (HTB-122)/ Hs 578T (HTB-126)/ MCF7 (HTB-22)/ ZR-75-1 (CRL-1500)/ BT-474 (HTB-20) and SK-BR-3 (HTB-30)) were obtained from American Type Culture Collection (ATCC; Manassas, VA, USA). The cells were authenticated through DNA profiling of eight different and highly polymorphic short-tandem repeat loci (DSMZ, Braunschweig, Germany) and were regularly tested for mycoplasma contamination. They were cultured in their recommended medium (ATCC) at 37 °C, 5% CO_2 and 95% humidity. Cells were used between passages 5 and 20 reaching near-confluence and were harvested with trypsin (Life Technologies, Carlsbad, CA, USA).

For transient silencing, cells were transfected using Lipofectamine (Cat. #: 11668-019; Life Technologies) with small-interfering RNA (Thermo Scientific, Rockford, IL, USA). After 16 h, transfection medium was replaced by fresh culture medium (DMEM supplemented with 10% fetal bovine serum (MP Biomedicals, Santa Ana, CA, USA) and 5 mM glutamine (MP Biomedicals)) and experiments were performed 48–72 h later. SiRNAs directed against myoferlin (siRNA MYOF#1: 5'-CCCUGUCUGGAAUGAGA-3' and siRNA MYOF#2: 5'-CGGCGGAUGCUGUCAAAUA-3') were used at a concentration of 10 nmol/l (Eurogentec, Liège, Belgium). ON-TARGETplus Non-Targeting Pool siRNA (GE Healthcare Dharmacon, PA, USA) was used as a negative control (further referred to as Irrelevant (Irr) siRNA).

For stable myoferlin silencing, MDA-MB-231 cells were transduced with lentiviral shRNA particles. shRNA plasmid targeting myoferlin (sequence 5'-CCCUGUCUGGAAUGAGA-3' cloned into pLKO, Sigma, St Louis, MO, USA) and control shRNA (Cat. #: SHC005; Sigma) were used. Lentiviral vectors were generated as follows: lenti-X 293T cells (Clontech, Mountain view, CA, USA) were co-transfected with shRNA, pSPAX2 (Addgene, Cambridge, MA, USA) and a VSV-G encoding plasmids. Viral supernatants were collected 48, 72 and 96 h post transfection, filtrated and concentrated 100x by ultracentrifugation. The lentiviral vectors were titrated with qPCR Lentivirus Titration (Titer) Kit (Cat. #: LV900; ABM, Richmond, BC, Canada). Following this, MDA-MB-231 cells were stably transduced with control and anti-myoferlin shRNA lentiviral vectors and the stably transduced clones were isolated by treatment with 10 μg/ml of Puromycin (ant-pr-1, Invivogen, Toulouse, France). To avoid clone-specific effects, pooled cultures were used for all the experiments. Cells that were used in murine *in vivo* experiments were additionally transduced with lentiviral vector to express the luciferase gene.

Murine xenograft-based tumor model

All animal experiments undertaken in this study were performed in accordance with the ARRIVE ethical guidelines[41] and were reviewed and approved by the Institutional Animal Care and Ethics Committee of the University of Liège (Belgium) (LA number 1610002, protocol number ULG1316). MR imaging[42] protocol used in the present study was approved by the Institutional Animal Care and Ethics Committee of the Center for Microscopy and Molecular Imaging (Gosselies, Belgium) (LA number 1500589, protocol number CMMI-2011-07). Female NOD-SCID mice were purchased from Janvier Labs (Saint Berthevin Cedex, France) and housed in the animal facility of the University of Liege under standard conditions (12 h light/dark cycle, lights on at 0700 hours). They were acclimated to the room 1 week before the beginning of the experiment. Food and water were provided *ad libitum*. Ten animals per replicate and condition were estimated as sufficient to account for the biological variability. No specific inclusion/exclusion criteria were used and the animals were not randomized. The investigators were not blinded during the study.

The grafting was conducted as follows: one million of MDA-MB-231 cells suspended in culture medium (DMEM supplemented with 10% fetal bovine serum and 5 mM glutamine) mixed 1:1 with Growth Factor Reduced Matrigel (Cat. #: 354230; BD Biosciences) were injected subcutaneously in the flank of 6-week-old female NOD-SCID mice. Tumor growth was weekly measured using a digital caliper and the volume was assessed using the formula $V = (4/3).\pi.(H/2).(L/2).(W/2)$ where H, L and W denote height, length and width of the tumor. After 4 weeks of development, tumors were removed and mice were observed during 4 additional weeks for the development of lung metastases. Monitoring for metastases was performed at 2 weeks post resection using MRI and at 4 weeks using histology following the sacrifice of the animals.

Magnetic resonance imaging of xenografted mice

Magnetic resonance imaging was performed on a 9.4 T Biospec (Bruker, Ettlingen, Germany) using a volume coil (38 mm diameter). Animals were kept anesthetized with 1–1.5% isoflurane delivered in oxygen. Their respiratory rate was monitored during the entire imaging session. T_2-weighted TurboRARE sequences were used: 20 coronal slices of 1mm thickness with repetition time: 2500 ms, echo time: 40.2 ms, 0.1 × 0.116 mm resolution, number of excitations: 8; and 40 axial slices of 1mm thickness with TR: 4845.4 ms, echo time: 40.2 ms, 0.1x0.104 mm resolution, number of excitations: 8. Using the VivoQuant software (Invicro, Boston, MA, USA) tumors were manually contoured on each slice and their volume was calculated.

Proteomic analysis of the xenografted tumors

All reagents used for proteomic analysis, unless otherwise specified, were purchased from Sigma. Snap-frozen tumors were pulverized and then lysed using RIPA buffer (50 mM Tris-HCl, pH 7.5, 150 mM NaCl, 1% Triton X-100, 0.5% Na deoxycholate, 0.2% SDS, supplemented with protease and phosphatase inhibitors). Three individual tumor lysates were pooled together and analyzed in triplicates. Protein extracts were further reduced with 100 mM dithiothreitol (Cat. #: D0632), alkylated with 150 mM of chloroacetamide (Cat. #: 22788) and precipitated with 20% trichloroacetic acid. Protein pellets were then suspended in ammonium bicarbonate buffer (50 mM NH_4CO_3, pH 8.0) and digested with trypsin (sequencing grade, 1/50: protease/protein; Promega). Finally, 5 µg of peptides were desalted using C18 ZipTip (Cat. #: ZTC18S096; Millipore, Billerica, MA, USA) and 2.5 µg were injected onto the 2D-nano Aquity ultra performance liquid chromatography (Waters, Milford, MA, USA) coupled online with the SYNAPT G2 qTOF system (Waters). Samples were loaded at 2 µl/min (20 mM ammonium formiate, pH 10) on a first dimension separation column X-Bridge BEH C18 5 µm (300 µm × 50 mm, Waters) and eluted using five steps (10, 14, 16, 20 and 65% acetonitrile). Each fraction was desalted on a trap column Symmetry C18 5 µm (180 µm × 20 mm, Waters) and separated on an analytical column BEH C18 1.7 µm (75 µm × 150 mm, Waters). Solvent A (0.1% formic acid in water) and solvent B (0.1% formic acid in acetonitrile) were mixed at a flow rate of 300 nl/min (gradient : 0 min, 97% A; 90 min, 60% A). Mass spectrometry data were acquired using alternate scanning mode, 50–1500 *m/z* range, ESI+, V optics, scan time 1 s, cone 30 V and lock mass [Glu1]-Fibrinopeptide B ($[M+2H]^{2+}$ 785.8426 *m/z*). Protein identifications and quantifications were conducted using ProteinLynx Global SERVER (PLGS) v2.4 using UniProt human database. Peptide modification carbamidomethylation was set as fixed and oxidation (M) as variable.

Metabolomic analysis of the xenografted tumors

Snap-frozen tumor samples were crushed and solubilized (sonicated) in 1ml of methanol (Wako, Tokyo, Japan). The samples were then split into two separate vials, each containing 0.5 ml of initial solution: (i) general metabolites and (ii) lipid mediators. For general metabolites analysis the samples were spiked with two internal standards: L-methionine sulfone (Cat. #: 502-76641; Wako) and 2-morpholinoethanesulfonic acid (Cat. #: 341-01622; Dojindo, Tokyo, Japan). Each standard was spiked at 10 µM final concentration. The general metabolites samples were further prepared by adding 250 µl of ultrapure water and 500 µl of chloroform (Wako). The sample mix was first vortexed vigorously followed by centrifugation at 15 000 *g* for 15 min/4 °C. The clear upper phase was removed and filtrated through a 5 kDa-cutoff filter (Vivaspin 500; GE Healthcare, Chicago, IL, USA) for 90 min/4 °C at 15 000 *g*. The filtrate was lyophilized and then dissolved in 100 µl of ultrapure water. About 3 µl of prepared general metabolites sample was then injected on ultra performance liquid chromatography coupled to triple-quadrupole MS (LCMS-8050; Shimadzu, Kyoto, Japan). The chromatographic conditions were as follows: analytical column Discovery HS F5-3 (Cat. #: 567503-U; Sigma-Aldrich, St Louis, MO, USA), mobile phase A 0.1% formic acid in water (Wako), mobile phase B 0.1% formic acid in acetonitrile (Wako), flow rate 0.25 ml/min, column oven 40 °C. The gradient was: 0–2 min 100% A, 5 min 75% A, 11 min 65% A, 15–20 min 5% A, 20.1–25 min 100% A. MS setting, data acquisition and data analysis were performed according to manufacturer instructions for analysing Primary Metabolites version 2.0 (Cat. #: 225-24865A, Shimadzu).

For lipid mediators analysis the samples were spiked with 16 internal standards: tetranor-PGEM-d6, 6-keto-PGF1a-d4, TXB2-d4, PGF2a-d4, PGE2-d4, PGD2-d4, LTC4-d5, LTB4-d4, 15-HETE-d8, 12-HETE-d8, 5-HETE-d8, PAF-d4, OEA-d4, EPA-d5, DHA-d5, DHA-d5 and AA-d8 (all purchased from Cayman Chemicals, Ann Arbor, MI, USA). Each standard was spiked at 30 µM final concentration. The samples were further incubated at 4 °C for 2 h under occasional vortexing, followed by centrifugation at 15 000 *g* for 10 min. The supernatant was removed and loaded on the Strata-X column (Phenomenex, Torrance, CA, USA). The column was washed with 1 ml 0.1% formic acid, 1 ml 15% ethanol and the compounds were eluted in 250 µl methanol. The eluate was lyophilized and then solubilized in 10 µl methanol final volume. Of this, 5 µl sample was injected on ultra performance liquid chromatography coupled to triple-quadrupole MS (LCMS-8050). The chromatographic conditions were as follows: analytical column Kinetex C8 (Cat. #: 00F-4497-AN; Phenomenex), mobile phase A 0.1% formic acid in water (Wako), mobile phase B acetonitrile (Wako), flow rate 0.4 ml/min, column oven 40 °C. The gradient was: 0 min 90% A, 5 min 75% A, 10 min 65% A, 20 min 25% A, 20.1–25 min 5% A, 25.1 min 90% A. MS setting, data acquisition and data analysis were performed according to manufacturer instructions for analysing Lipid Mediators version 2.0 (Cat. #: 225-24873A, Shimadzu).

Histology, immunofluorescence and IHC

Formalin-fixed paraffin-embedded breast tissue sections (5 µm) were dewaxed three times in xylene and sequentially rehydrated in baths of decreasing methanol content (100/95/70/50%). The slides were then incubated with 3% H_2O_2 in 90% methanol for 30 min to ensure blocking of endogenous peroxidase. For immunofluorescence, the slides were blocked and stained using the anti-myoferlin, anti-pAMPK and anti-HIF1A antibodies as instructed in the TSA fluorescent kit (Perkin Elmer, Billerica, MA, USA). For IHC, the slides were incubated for 30 min in 1.5% normal serum (Vector Laboratories, Burlingame, CA, USA). Primary antibody incubation was performed overnight at 4 °C (antibody dilution was 1/100 for anti-myoferlin, whereas anti-vimentin was obtained as a ready-to-use solution) and followed by successive washes in phosphate-buffered saline (PBS). Anti-myoferlin antibody was purchased from Sigma-Aldrich (Cat. #: HPA014245) and anti-vimentin was obtained from Ventana (Cat. #: 790-2917; Tucson, AZ, USA). Next, the slides were incubated for 30 min with corresponding biotinylated anti-rabbit secondary antibodies (Vector Laboratories), stained with avidin-biotin-complex kit (Vectastain ABC kit, Vector Laboratories) for an additional 30 min and colored with 3,3′-diaminobenzidine tetrachlorhydrate dehydrate and 5% H_2O_2. Finally, the slides were counter-stained with hematoxylin. Two independent evaluators (PD and AT) examined tissue positivity in a blinded fashion and using a semi-quantitative approach. The samples were scored for the percentage of positivity (divided into three classes: 1 = 0–33%, 2 = 33–66% and 3 = 66–100%) and for intensity (0 = no staining, 1 = weak, 2 = moderate and 3 = strong). Following this, both parameters were multiplied and yielded a unique score. Sections of xenografted tumors were examined histologically using hematoxylin/eosin staining. The vimentin staining was used to identify tumor cells in mice xenografts (both in primary tumors and lungs) and was also performed on paraffin-embedded tissues. The number and the size of metastatic foci were evaluated and quantified using vimentin staining.

Western blot

Cell pellets were lysed in SDS-based buffer (50 mM Tris-HCL, 1% SDS, pH 7.5, supplemented with protease and phosphatase inhibitors, complete EDTA free, (Cat. #: 11873580001; Roche, Mannheim, Germany)) and pulverized tissue samples were solubilized in RIPA buffer (50 mM Tris-HCl, pH 7.5, 150 mM NaCl, 1% Triton X-100, 0.5% Na deoxycholate, 0.2% SDS, supplemented with protease and phosphatase inhibitors, complete EDTA free, (Cat. #: 11873580001; Roche)). Protein quantification was performed using the BCA quantification kit (Thermo Scientific). Twenty microgram of proteins were mixed with Laemmli buffer (60 mM Tris-HCl pH 6.8, 25% glycerol, 2% SDS, 14.4 mM of 2-mercaptoethanol and trace of bromophenol blue) and denatured for 5 min at 99 °C. Protein samples were loaded and separated by SDS–PAGE followed by electro-transfer on PVDF membrane. The membranes were incubated with the selected primary antibodies (outlined below) overnight at 4 °C and then probed with corresponding secondary antibody conjugated to horseradish peroxidase (anti-rabbit antibody (Cat. #: G21234; Life Technologies) and anti-mouse antibody (Cat. #: P0260; Dako, Glostrup, Denmark)) for 1 h at room temperature. Finally, the immunoblots were revealed using the chemiluminescent substrate (ECL Western blotting substrate, Thermo Scientific).

Myoferlin was detected using the antibody described above (Cat. #: HPA014245; Sigma-Aldrich). Antibodies against AMPK (Cat. #: 2795), pAMPK (Cat. #: 2535), p-ACC (Cat. #: 3661) were purchased from Cell Signaling (Danvers, MA, USA). PDH (Cat. #: ab168379), pPDH (Cat. #: ab92696), PDHK1 (Cat. #: ab47987) were purchased from Abcam (Cambridge, UK). Anti-COX1 was purchased from Life Technologies, Carlsbad, CA, USA (Cat. #: 459600), anti-HIF1A from BD Biosciences (Cat. #: 610958; San Jose, CA, USA), vimentin (Cat. #: v6389) was obtained from Sigma-Aldrich. Anti NDUFB5 was obtained from Genetex (Cat. #: GTX111880; Irvine, CA, USA) and anti-mitofilin from Santa Cruz (Cat. #: sc-390707, Dallas, TX, USA). HSC70 (Cat. #: sc-7298; Santa Cruz) was used as a loading control.

Electron microscopy and immunogold labeling

MDA-MB-231 cells were fixed for 30 min in 2.5% glutaraldehyde (diluted in Sorensen's buffer: 0.1 M Na_2HPO_4/NaH_2PO_4 buffer, pH 7.4) at 4 °C and postfixed in 2% OsO_4 (diluted in Sorensen's Buffer 0.1 M). After dehydration in graded ethanol, samples were embedded in Epon resin (Sigma-Aldrich).

Ultrathin sections obtained with a Reichert Ultracut S ultramicrotome (Reichert Technologies, Depew, NY, USA) were contrasted with 2% uranyl acetate and 4% lead citrate. Observations were made with a Jeol JEM-1400 transmission electron microscope at 80 kV (Jeol, Peabody, MA, USA).

For immunolabeling, samples were first fixed for 1 h in 4% formaldehyde (diluted in Sorensen's buffer 0.1M), rinsed in buffer and dehydrated in graded ethanol baths. After dehydration, samples were infiltrated with increasing concentrations of Lowicryl K4M resin. Resin was further polymerized under ultraviolet light. Ultrathin sections were washed in phosphate buffer saline (0.1 M PBS, 0.14 M NaCl, 6 mM Na_2HPO_4, 4 mM KH_2PO_4, pH 7.2) then blocked for 30 min in PBS-BSA (1%, pH 7.2) supplemented with normal goat serum (1/30 dilution). Sections were washed in PBS-BSA (0.2%, pH 7.2) and incubated with primary antibody (anti-MYOF, 1/20 dilution in PBS-BSA 0.2% supplemented with normal goat serum 1/50) for 3 h. After three washes in PBS-BSA (1%, pH 7.2) and an additional wash in PBS-BSA (0.2%, pH 8.2), sections were incubated with secondary antibody (anti-rabbit coupled with gold particles of 10 nm size (Aurion, Wageningen, The Netherlands) diluted 1/40 in PBS-BSA 0.2%, pH 8.2) for 1 h. Finally, sections were washed four times in PBS-BSA (0.2%, pH 8.2) and four times in deionized water, stained with uranyl acetate and lead citrate and allowed to dry. Observations were made with a Jeol JEM-1400 transmission electron microscope at 80 kV (Jeol).

Nuclear magnetic resonance-based metabolomics

The NMR spectra were recorded at 298 K on a Bruker Avance spectrometer (Bruker) operating at 500.13 MHz for proton and equipped with a TCI cryoprobe (Bruker). Deuterium oxide (99.96% D), deuterated chloroform (99.8% D) and trimethylsilyl-3-propionic acid-*d*4 were purchased from Eurisotop (St-Aubin, France), phosphate buffer powder 0.1 M and maleic acid were purchased from Sigma-Aldrich. Deuterated solvents were used as the internal lock. The data have been processed with Bruker TOSPIN 3.0 (Bruker) software with standard parameter set. Phase and baseline correction were performed manually over the entire range of the spectra and the δ scale was calibrated to 0 ppm using the internal standard trimethylsilyl-3-propionic acid-*d*4 (TMSP). One million cells were lysed by sonication according to a described procedure.[43] About 500 µl of cell lysates were supplemented with 100 µl of deuterated phosphate buffer (pH 7.4), 100 µl of a 5 mM solution of maleic acid and 10 µl of a 10 mg/ml TMSP D_2O solution. The sample was distributed into 5-mm tubes for NMR measurement. ^{1}H NMR spectra were acquired using a 1D NOESY sequence with presaturation. The Noesypresat experiment used a relaxation delay-90°-t1-90°-tm-90°-acquire sequence with a relaxation delay of 4 s, a mixing time tm of 10 ms and a fixed t1 delay of 4 µs. Water suppression pulse was placed during the relaxation delay. The number of transient was 32 (64K data points) and a number of four dummy scans was chosen. Acquisition time was fixed to 3.2769001 s.

For extracellular lactate dosage, 500 µl of collected conditioned culture media were supplemented with 100 µl of deuterated phosphate buffer (pH 7.4), 100 µl of a 35 mM solution of maleic acid and 10 µl of TMSP. The solution was distributed into 5-mm tubes for NMR measurement. ^{1}H NMR spectra were acquired using a 1D NOESY sequence with presaturation and 32 transients and 4 dummy scans. Lactate concentration was obtained by integrations of the lactate signal at 1.34 ppm using maleic acid as internal standard.

For lipid quantification, lipid-enriched fraction of cancer cells was obtained after incubation in chloroform. The cell pellets were suspended in 250 µl of water, vortexed for 1 min and then supplemented with 500 µl of deuterated chloroform ($CDCl_3$). The mixture was vortexed for 1 min, supplemented with 500 µl of deuterated chloroform ($CDCl_3$) and 650 µl of water and stirred at 300 rpm during 10 min at 4 °C. The sample was then centrifuged (12 000 *g*, 5 min, 4 °C) to eliminate the membranes and the cell residues and the organic layer were collected. About 200 µl of $CDCl_3$ containing 0.03% of tetramethylsilane was added to 500 µl of this solution. The mixture was transferred into 5-mm NMR tubes and a proton spectrum was acquired with 32 transients and 4 dummy scans. Relative lipid dosages were achieved by integrations of the lactate signal around 0.85 ppm using tetramethylsilane as internal standard.

For metabolomics analysis, the optimized 1H-NMR spectra were automatically baseline corrected and reduced to ASCII files using the AMIX software (Bruker, Version 3.9). The spectral intensities were normalized to the total intensities and reduced to integrated regions of equal width (0.04 ppm) corresponding to the a 0.5–10.00 ppm region. Because of the residual water signal, the region between 4.5 and 6.1 ppm was removed prior to further analysis. The matrices obtained were used for the statistical analysis. The reduced and normalized NMR spectral data were imported into SIMCA (version 13.0.3, Umetrics AB, Umea, Sweden) in order to perform discriminant analysis (principal component analysis). SIMCA was used to generate all principal component analysis score and loading plots.

Gas chromatograpy-based quantification of free fatty acids

Twenty million cells were pelleted, subjected to three freeze and thaw cycles and further resuspended in 300 µl of PBS. Cell lysates were then diluted in a 95/5 methanol/HCl solution, mixed and incubated for 1 h at 105 °C. Next, cell suspension was diluted in an hexane solution (4/10 ratio), mixed on a rotatory shaker for 10 min and centrifuged for 10 min at 2000 *g*. The organic phase was collected with a glass pipette, allowed to evaporate under N_2 flux and finally suspended in 100 µl of hexane. Samples were analysed on a Shimadzu GC-2010 (Shimadzu). Synthetic C28 (Sigma-Aldrich) was added as an internal standard to allow absolute quantification of the samples. Analysis and quantification of the different free fatty acid subclasses was performed using the GCSolution Analysis 2.3 software (Shimadzu). Results for myoferlin-depleted cells were expressed as percentage of control cells (set at 100%).

WST-1 assay

Forty-eight or seventy-two hours after transfection, WST-1 reagent (Cat. #: HPA014245; Roche) was diluted 1/10 in the culture medium of living cells, according to manufacturer's instructions. Absorbance at 450 nm was then measured after 30, 60 and 120 min of incubation using a Multiskan MS Elisa Plate Reader (Thermo Scientific).

Isolation of mitochondria

MDA-MB-231 cells were washed with PBS, trypsinized and suspended in cold washing buffer (250 mM Sucrose, 1 mM EDTA, 10 mM Tris, pH 7.4). Cells were then centrifuged for 5 min at 200 g and further suspended in buffer A (250 mM Sucrose, 1 mM EDTA, 24 mM Tris, pH 7.4 supplemented with protease inhibitors (complete EDTA free, (Roche) and 0.5 mg bovine serum albumin)). Cells were crushed using a glass/teflon tissue grinder and the cell lysate was centrifuged for 3 min at 750 g. The supernatant was collected and enriched fraction of mitochondria was obtained after 3 min of high-speed centrifugation at 13 000 *g*. Mitochondrial pellet was washed once with buffer B (250 mM sucrose, 1 mM EDTA, 24 mM Tris, pH 7.4 supplemented with protease inhibitors (complete EDTA free, Roche)) to eliminate BSA, centrifuged for 3 min at 11 000 *g* and finally suspended in 200 µl of buffer B. Further purification of isolated mitochondria was conducted using sucrose gradient ultracentrifugation. Briefly, mitochondrial suspension was deposited on the top of a discontinuous sucrose gradient (60–32–23%). After 1 h ultracentrifugation (Beckmann Optima LE-80K, Krefeld, Germany) at 125 000 *g*, mitochondria were collected at the interface between the 60 and 32% sucrose layers. Sucrose was sequentially eliminated after several washes with buffer B followed by centrifugation at 13 000 *g*. Mitochondrial pellet was suspended in appropriate volume of lysis buffer (50 mM Tris-HCL, 1% SDS, pH 7.5, supplemented with protease and phosphatase inhibitors).

Oxygen consumption measurements

Forty-eight hours post transfection, the cells were subjected to oxygen consumption analysis using high-resolution oxygraph (Oroboros Instruments, Innsbruck, Austria) with a Clarke electrode at 37 °C. Five millions cells (MDA-MB-231 and MDA-MB-468) or fifteen millions cells (isolated cells from tumor xenografts) were used for each measurement. The measurement was performed under continuous stirring. Routine respiration was measured in culture medium. Leak respiration, which corresponds to the proportion of oxygen that is consumed by the cell without producing ATP, was measured in the presence of 5 µM oligomycin. ETSmax (electron transport system), reflecting the maximal capacity of the mitochondrial respiratory chain, was obtained in presence of 0.5 µM of the uncoupling agent FCCP (three pulses of FCCP were made to ensure maximal uncoupling of the respiratory chain). All respiration measurements were corrected for residual oxygen consumption measured in presence of 2.5 µM of rotenone. The slopes of O_2 consumption, representing the routine respiration of the cells, were calculated with the Oroboros oxygraph software (DatLab 4.0, Oroboros Instruments, Innsbruck, Austria). Routine, leak and ETSmax respiration of control cells were set at 100% and compared with measurements obtained following myoferlin silencing.

Apoptosis assay

Myoferlin-silenced cells were collected in serum medium at selected time points. Apoptosis was evaluated using the FITC Annexin-V Apoptosis Detection Kit I (Cat. #: 556547; BD Pharmingen, San Diego, CA, USA) according to the manufacturer's instructions. Briefly, adherent and floating cells were collected, pelleted, washed twice with ice-cold PBS and incubated in the dark with Annexin-FITC and propidium iodide (PI) for 15 min. Flow cytometry was performed using a FACS-Calibur 2 (BD, San Jose, CA, USA). Data were evaluated using the CellQuest Pro software (BD). Early (Annexin-V^+/PI^-) and late (Annexin-V^+/PI^+) apoptotic populations were summed to evaluate apoptosis.

Mitochondrial membrane potential measurement

Adherent and floating cells were collected, pelleted, washed twice with ice-cold PBS and incubated with the tetra-methyl-rodhamin-ester (TMRE) dye (100 nM final concentration, Ref.: ab113852, Abcam) for 20 min in culture medium without serum. Cells were then washed once with ice-cold PBS and resuspended in PBS. Fluorescence signal was analyzed using a FACS-Calibur 2 (BD). Two peaks were observable corresponding to depolarized and functional mitochondria. The percentage of each population was evaluated using the CellQuest Pro software (BD).

ATP measurement

Intracellular ATP was measured using ApoSENSOR ADP/ATP Ratio Assay Kit from BioVision (Cat. #: K255-200; San Francisco, CA, USA) according to manufacturer's instructions. Briefly, transfected cells were washed and lysed in nucleotide releasing buffer for 5 min. Solution was then mixed with ATP monitoring enzyme solution (coupled with luciferase) and allowed to react for 2 min. Luminescence was measured using the Lumat LB 9507 (Berthold Technologies, Vilvoorde, Belgium) and the results were expressed as relative percentages in relationship to the values obtained with control cells.

ROS measurement

Breast cancer cells were trypsinized, collected and incubated with MitosoxRed (5 μM; Life Technologies) for 20 min in HBSS buffer. Cells were then washed once with ice-cold PBS and resuspended in PBS. Fluorescence signal was accrued using a FACS-Calibur 2 (BD). Data were evaluated using the CellQuest Pro software (BD). Median fluorescence intensity of control cells was set at 100%.

Dichloroacetic acid and compound C treatment of cancer cells

Sixteen hours post transfection, culture medium was changed and DCA (Cat. #: D54702; Sigma-Aldrich) was added at a final concentration of 10 mM. Apoptosis and mitochondrial depolarization were assessed 72 h later. Compound C (dorsomorphin, Sigma-Aldrich) was added 48 h post transfection to the cells in fresh culture medium at a final concentration of 5 μM. Effect on apoptosis and mitochondrial depolarization were monitored 24 h later.

Statistical analysis

For all studies except IHC, statistical analysis was conducted using two-sided Student's *t*-test and assuming equal variances (Excel; Microsoft, Redmond, WA, USA). The *t*-test was used because data followed a normal distribution (Shapiro–Wilk test, threshold 0.05). For IHC evaluation, Box plots were generated using Sigma Plot software (Systat Software, Inc., Chicago, IL, USA; version 10.0). Statistical significance of the myoferlin expression was assessed using Mann–Whitney *U*-test as the data did not follow normal distribution. The number of biological replicates is described in the figure legends.

Survival analysis

Kaplan–Meier survival curves were plotted using publicly available online tools KM plotter (http://kmplot.com/analysis). The statistical analysis was conducted as described elsewhere.[44]

CONFLICT OF INTEREST

The authors declare no conflict of interest.

ACKNOWLEDGEMENTS

We acknowledge the experimental support of Dr Chantal Humblet and Mrs Alice Marquet (GIGA-histology platform, ULg), Dr Sandra Ormenese (GIGA-imaging platform, ULg), Mr Vincent Hennequière and Mrs Naima Maloujahmoum (Metastasis Research Laboratory) for experimental support. We are also thankful to the institutional Biobank of the University Hospital Liege for providing patient material. Mr Mathieu Roch (CMMI) is thanked for his help in tumor volume measurements on MR images. We are grateful to Mrs Marie-Aline Laute and Mr Nicolas Passon, the Cyclotron team (Erasme Hospital, Brussels, Belgium) and Dr. Bolag Altan (Gunma University) for technical assistance. The results shown in this work are in part based upon data generated by the TCGA Research Network: http://cancergenome.nih.gov/. This work was supported with grants from the University of Liège (Concerted Research Action Program (IDEA project)), National Fund for Scientific Research (FNRS), Fonds Erasme, Convention de Recherche Association Vinçotte Nuclear—AVN and Gunma University (GIAR Research Program for Omics-Based Medical Science). Andrei Turtoi and Arnaud Blomme are post-doctoral research fellows (FNRS/Televie), Akeila Bellahcène and Pascal de Tullio are senior research associates (FNRS). The Center for Microscopy and Molecular Imaging (CMMI) as well as Gilles Doumont are supported by the European Regional Development Fund and Wallonia (FEDER). No funding bodies had any role in study design, data collection and analysis, decision to publish or preparation of the manuscript.

REFERENCES

1 Liedtke C, Mazouni C, Hess KR, Andre F, Tordai A, Mejia JA *et al.* Response to neoadjuvant therapy and long-term survival in patients with triple-negative breast cancer. *J Clin Oncol* 2008; **26**: 1275–1281.
2 Mayer IA, Abramson VG, Lehmann BD, Pietenpol JA. New strategies for triple-negative breast cancer--deciphering the heterogeneity. *Clin Cancer Res* 2014; **20**: 782–790.
3 O'Toole SA, Beith JM, Millar EK, West R, McLean A, Cazet A *et al.* Therapeutic targets in triple negative breast cancer. *J Clin Pathol* 2013; **66**: 530–542.
4 Vander Heiden MG. Targeting cancer metabolism: a therapeutic window opens. *Nat Rev Drug Discov* 2011; **10**: 671–684.
5 Warburg O. On the origin of cancer cells. *Science* 1956; **123**: 309–314.
6 Jose C, Bellance N, Rossignol R. Choosing between glycolysis and oxidative phosphorylation: a tumor's dilemma? *Biochim Biophys Acta* 2011; **1807**: 552–561.
7 Zheng J. Energy metabolism of cancer: glycolysis versus oxidative phosphorylation (Review). *Oncol Lett* 2012; **4**: 1151–1157.
8 Griguer CE, Oliva CR, Gillespie GY. Glucose metabolism heterogeneity in human and mouse malignant glioma cell lines. *J Neurooncol* 2005; **74**: 123–133.
9 Miccheli A, Tomassini A, Puccetti C, Valerio M, Peluso G, Tuccillo F *et al.* Metabolic profiling by 13C-NMR spectroscopy: [1,2-13C2]glucose reveals a heterogeneous metabolism in human leukemia T cells. *Biochimie* 2006; **88**: 437–448.
10 Chen JL, Lucas JE, Schroeder T, Mori S, Wu J, Nevins J *et al.* The genomic analysis of lactic acidosis and acidosis response in human cancers. *PLoS Genet* 2008; **4**: e1000293.
11 Haq R, Shoag J, Andreu-Perez P, Yokoyama S, Edelman H, Rowe GC *et al.* Oncogenic BRAF regulates oxidative metabolism via PGC1alpha and MITF. *Cancer Cell* 2013; **23**: 302–315.
12 Sorkin A, von Zastrow M. Endocytosis and signalling: intertwining molecular networks. *Nat Rev Mol Cell Biol* 2009; **10**: 609–622.
13 Goldstein JL, Brown MS. The LDL receptor. *Arterioscler Thromb Vasc Biol* 2009; **29**: 431–438.
14 Aisen P, Enns C, Wessling-Resnick M. Chemistry and biology of eukaryotic iron metabolism. *Int J Biochem Cell Biol* 2001; **33**: 940–959.
15 Jovic M, Sharma M, Rahajeng J, Caplan S. The early endosome: a busy sorting station for proteins at the crossroads. *Histol Histopathol* 2010; **25**: 99–112.
16 Antonescu CN, McGraw TE, Klip A. Reciprocal regulation of endocytosis and metabolism. *Cold Spring Harb Perspect Biol* 2014; **6**: a016964.
17 Rambold AS, Cohen S, Lippincott-Schwartz J. Fatty acid trafficking in starved cells: regulation by lipid droplet lipolysis, autophagy, and mitochondrial fusion dynamics. *Dev Cell* 2015; **32**: 678–692.
18 Unger RH, Clark GO, Scherer PE, Orci L. Lipid homeostasis, lipotoxicity and the metabolic syndrome. *Biochim Biophys Acta* 2010; **1801**: 209–214.
19 Li R, Ackerman WEt, Mihai C, Volakis LI, Ghadiali S, Kniss DA. Myoferlin depletion in breast cancer cells promotes mesenchymal to epithelial shape change and stalls invasion. *PLoS One* 2012; **7**: e39766.
20 Turtoi A, Blomme A, Bellahcene A, Gilles C, Hennequiere V, Peixoto P *et al.* Myoferlin is a key regulator of EGFR activity in breast cancer. *Cancer Res* 2013; **73**: 5438–5448.
21 Volakis LI, Li R, Ackerman WEt, Mihai C, Bechel M, Summerfield TL *et al.* Loss of myoferlin redirects breast cancer cell motility towards collective migration. *PLoS One* 2014; **9**: e86110.

22 Sachen KL, Strohman MJ, Singletary J, Alizadeh AA, Kattah NH, Lossos C *et al.* Self-antigen recognition by follicular lymphoma B-cell receptors. *Blood* 2012; **120**: 4182–4190.
23 Turtoi A, Musmeci D, Wang Y, Dumont B, Somja J, Bevilacqua G *et al.* Identification of novel accessible proteins bearing diagnostic and therapeutic potential in human pancreatic ductal adenocarcinoma. *J Proteome Res* 2011; **10**: 4302–4313.
24 Wang WS, Liu XH, Liu LX, Lou WH, Jin DY, Yang PY *et al.* iTRAQ-based quantitative proteomics reveals myoferlin as a novel prognostic predictor in pancreatic adenocarcinoma. *J Proteomics* 2013; **91**: 453–465.
25 Fahmy K, Gonzalez A, Arafa M, Peixoto P, Bellahcene A, Turtoi A *et al.* Myoferlin plays a key role in VEGFA secretion and impacts tumor-associated angiogenesis in human pancreas cancer. *Int J Cancer* 2016; **138**: 652–663.
26 Leung C, Yu C, Lin MI, Tognon C, Bernatchez P. Expression of myoferlin in human and murine carcinoma tumors: role in membrane repair, cell proliferation, and tumorigenesis. *Am J Pathol* 2013; **182**: 1900–1909.
27 Doherty KR, Demonbreun AR, Wallace GQ, Cave A, Posey AD, Heretis K *et al.* The endocytic recycling protein EHD2 interacts with myoferlin to regulate myoblast fusion. *J Biol Chem* 2008; **283**: 20252–20260.
28 Bernatchez PN, Sharma A, Kodaman P, Sessa WC. Myoferlin is critical for endocytosis in endothelial cells. *Am J Physiol Cell Physiol* 2009; **297**: C484–C492.
29 Bernatchez PN, Acevedo L, Fernandez-Hernando C, Murata T, Chalouni C, Kim J *et al.* Myoferlin regulates vascular endothelial growth factor receptor-2 stability and function. *J Biol Chem* 2007; **282**: 30745–30753.
30 Neve RM, Chin K, Fridlyand J, Yeh J, Baehner FL, Fevr T *et al.* A collection of breast cancer cell lines for the study of functionally distinct cancer subtypes. *Cancer Cell* 2006; **10**: 515–527.
31 Kiss AL. Caveolae and the regulation of endocytosis. *Adv Exp Med Biol* 2012; **729**: 14–28.
32 Penzo D, Tagliapietra C, Colonna R, Petronilli V, Bernardi P. Effects of fatty acids on mitochondria: implications for cell death. *Biochim Biophys Acta* 2002; **1555**: 160–165.
33 Doherty KR, Cave A, Davis DB, Delmonte AJ, Posey A, Earley JU *et al.* Normal myoblast fusion requires myoferlin. *Development* 2005; **132**: 5565–5575.
34 Pilch PF, Liu L. Fat caves: caveolae, lipid trafficking and lipid metabolism in adipocytes. *Trends Endocrinol Metab* 2011; **22**: 318–324.
35 Hullin-Matsuda F, Taguchi T, Greimel P, Kobayashi T. Lipid compartmentalization in the endosome system. *Semin Cell Dev Biol* 2014; **31**: 48–56.
36 Pavlova NN, Thompson CB. The emerging hallmarks of cancer metabolism. *Cell Metab* 2016; **23**: 27–47.
37 LeBleu VS, O'Connell JT, Gonzalez Herrera KN, Wikman H, Pantel K, Haigis MC *et al.* PGC-1alpha mediates mitochondrial biogenesis and oxidative phosphorylation in cancer cells to promote metastasis. *Nat Cell Biol* 2014; **16**: 992–1003 1-15.
38 Porporato PE, Payen VL, Perez-Escuredo J, De Saedeleer CJ, Danhier P, Copetti T *et al.* A mitochondrial switch promotes tumor metastasis. *Cell Rep* 2014; **8**: 754–766.
39 DeBerardinis RJ, Lum JJ, Hatzivassiliou G, Thompson CB. The biology of cancer: metabolic reprogramming fuels cell growth and proliferation. *Cell Metab* 2008; **7**: 11–20.
40 Ward PS, Thompson CB. Metabolic reprogramming: a cancer hallmark even warburg did not anticipate. *Cancer Cell* 2012; **21**: 297–308.
41 Kilkenny C, Browne WJ, Cuthill IC, Emerson M, Altman DG. Improving bioscience research reporting: the ARRIVE guidelines for reporting animal research. *PLoS Biol* 2010; **8**: e1000412.
42 Youm YH, Nguyen KY, Grant RW, Goldberg EL, Bodogai M, Kim D *et al.* The ketone metabolite beta-hydroxybutyrate blocks NLRP3 inflammasome-mediated inflammatory disease. *Nat Med* 2015; **21**: 263–269.
43 Matheus N, Hansen S, Rozet E, Peixoto P, Maquoi E, Lambert V *et al.* An easy, convenient cell and tissue extraction protocol for nuclear magnetic resonance metabolomics. *Phytochem Anal* 2014; **25**: 342–349.
44 Gyorffy B, Surowiak P, Budczies J, Lanczky A. Online survival analysis software to assess the prognostic value of biomarkers using transcriptomic data in non-small-cell lung cancer. *PLoS One* 2013; **8**: e82241.

Supplementary Information accompanies this paper on the *Oncogene* website (http://www.nature.com/onc)